fluids

MDPI

Article

A Numerical Evaluation of Airborne Transmission Control through Saliva Modification

Rajendra Shrestha [1,*], Douglas Fontes [2] and Michael Kinzel [1,*]

[1] Department of Mechanical and Aerospace Engineering, University of Central Florida, Orlando, FL 32816, USA
[2] Physics and Engineering Department, Westmont College, Santa Barbara, CA 93108, USA; dfontes@westmont.edu
* Correspondence: rajendra.shrestha@ucf.edu (R.S.); michael.kinzel@ucf.edu (M.K.)

Abstract: The present study explored the relationship between airborne transmission and the saliva fluid properties of a human sneeze. Specifically, we aimed to understand if altering the saliva and its relationship to droplet breakup and stability can affect its transmission characteristics. The study aimed to answer this question using computational fluid dynamics, specifically, a hybrid Eulerian–Lagrangian model with a Spalart–Allmaras, detached eddy simulation turbulence model. The effort focused on a scenario with a sneeze event within a ventilated room. The study found that for sneezes, secondary breakdown processes are important. Thicker saliva that increased the Ohnesorge number displayed a clear resistance to aerosolization due to stabilized secondary breakup, leading the bulk of the drops having high settling rates that are less likely to drive airborne transmission. For instance, the use of xanthum gum, which increased the saliva viscosity by 2000%, reduced the formation of aerosols. Additionally, another class of modifiers that reduce saliva content was studied, which was also effective in reducing airborne transmission drivers. Zingiber, which reduced the saliva content, reduced the formation of aerosols. However, when considering the overall reduction in droplet volume, saliva modifiers such as cornstarch, xanthum gum, and lozenges increased the mean droplet size by 50%, 25%, and 50%, respectively, while reducing the overall droplet volume by 71.6%, 71.2%, and 77.2%, respectively. Conversely, Zingiber reduced the mean droplet size by 50% but increased the overall droplet volume by 165.7%. Overall, for this type of respiratory event, this study provides insight into the potential for modifying saliva characteristics that may impact airborne transmission and could introduce new tools for reducing airborne pathogen transmission.

Keywords: airborne transmission; Eulerian–Lagrangian CFD; saliva modification; sneezing; droplet breakup

check for updates

Citation: Shrestha, R.; Fontes, D.; Kinzel, M. A Numerical Evaluation of Airborne Transmission Control through Saliva Modification. *Fluids* **2024**, *9*, 228. https://doi.org/10.3390/fluids9100228

Academic Editor: Lin Tian

Received: 25 June 2024
Revised: 18 September 2024
Accepted: 22 September 2024
Published: 30 September 2024

Copyright: © 2024 by the authors. Licensee MDPI, Basel, Switzerland. This article is an open access article distributed under the terms and conditions of the Creative Commons Attribution (CC BY) license (https://creativecommons.org/licenses/by/4.0/).

1. Introduction

Airborne pathogens such as those that cause cold, influenza, and tuberculosis have persistently affected humans and animals. The Coronavirus Disease 2019 (COVID-19) pandemic caused by the severe acute respiratory syndrome coronavirus 2 (SARS-CoV-2) virus has emphasized the importance of studying the flow mechanisms associated with such pathogens. SARS-CoV-2 is a respiratory virus and the prominent factor that led to its global presence is its high rate of spread despite government mitigation efforts around the globe. With an estimated mortality rate of up to 3% [1] and more than 600 million documented cases of COVID-19 with more than 6 million deaths, developing such an understanding is critical. Such pathogens are encapsulated within droplets and/or aerosols that are released when a person sneezes, coughs, or breathes, driving much of the transmission [2].

Physically, this transmission process is sensitive to the creation of droplets during respiratory events, and their settling, evaporation, dispersion, and eventual inhalation [3]. Settling, evaporation, and dispersion are all linked to the droplet size, which, in the

atomization community, was established to be connected to the Weber number (We) and Ohnesorge number (Oh) [4–6], which are defined as

$$We = \frac{\rho U_{rel}^2 D}{\sigma}, \tag{1}$$

and

$$Oh = \frac{\mu_d}{\sqrt{\rho_d D \sigma}}. \tag{2}$$

Here, ρ is the density of the medium, ρ_d is the density of the droplet, U_{rel} represents the relative velocity magnitude between the droplet and flow medium, D is the droplet diameter, σ is the surface tension of the droplet, and μ_d is the droplet dynamic viscosity. These non-dimensional parameters are therefore critical to the flow physics of airborne transmission.

For settling rates, the ratio between the surface area (correlating to drag) and volume (correlating to weight) decreases as the droplet size increases. The result is that larger droplets tend to settle quicker but are also more likely to encapsulate a higher count of viral particles. Hence, large droplets are more desirable to prevent airborne transmission. Alternatively, the dynamics of smaller droplets are drag dominant, which causes them to loiter longer in the air and encourages evaporation and, therefore, they are more commonly aerosolized and have a larger relative drag, which makes them prone to suspension and airborne transmission. These competing effects are well described by Wells' curve, which plots the minimum settling and evaporation times as a function of droplet size [7]. Studies have shown that influenza and SARS-CoV-2 aerosols can remain active for up to (and potentially over) 2–3 h [8], providing time for transmission. Hence, in the context of airborne pathogens, droplet size is critical.

Previous studies have focused on studying the dispersion and settling of these droplets. Investigations into droplet size measurements have indicated that the range of droplet sizes varies from 1 to 2000 µm, with a peak of 8–16 µm for coughs and 4–8 µm for sneezes [3]. In one study using Optical Particle Counting (OPC), it was found that most droplets fell within the 0.09–3.0 µm range. However, OPC has limited capabilities in detecting smaller droplet sizes [3]. Alternative techniques like Aerodynamic Particle Sizing (APS) and Scanning Mobility Particles Sizing (SMPS) have been utilized and have shown that coughing generates droplets ranging from 0.58 to 5.42 µm, with 82% of the droplets concentrated between 0.74 and 2.12 µm. However, the accuracy of interferometric Mie imaging (IMI) techniques is restricted to smaller droplets within the 2–3 µm range [3,9–11].

A series of viral transmission studies exist that span from theoretical models to real-life scenarios, which evaluated the fluid dynamics and examined the sensitivity to physical parameters like temperature, air humidity, and ventilation [12–15]. Research using particle image velocimetry of cough droplets found that the low temperatures and high relative humidity typical of winter caused more droplets to settle on the ground [12]. A large eddy simulation model was used to evaluate the effectiveness of face coverings and social distancing in reducing transmission risk [13]. Additionally, a Eulerian–Lagrangian model of human sneezing in a room with varying relative humidity levels demonstrated that increased relative humidity reduces droplet evaporation and lowers the exposure to droplet transmission [15].

In terms of evaporation, Refs. [16,17] studied evaporation-induced shear stresses on droplets, which were found to vary from 0.00025 to 0.02 Pa (mostly due to diffusion and Marangoni flow), which are insufficient to disrupt the virus. Hence, minimization of the drying time of virus-laden droplets is highly recommended to kill the virus. However, this research was focused on the evaporation of droplets stuck on walls. Since the life span of a virus is dependent on the wettability of droplets, aerosol transmission can be reduced with heating, ventilation, and air conditioning (HVAC) systems, opening windows, and installing glass barriers [18–24]. Experiments and numerical modeling studying the effects of crossflow ventilation on droplet diffusion demonstrated that crossflow effectively reduces the axial displacement of droplets during respiratory events [18]. The steady-state

Reynolds-averaged Navier–Stokes k-epsilon modeling of aerosol dispersion, compared with optical particle sizer experiments, highlights the significance of aerosol recirculation in limiting airborne transmission [19]. Similar CFD modeling results from a human volunteer, compared with particle image velocimetry results, revealed a reduction in plume buoyancy due to thermal stratification of the room [20]. CFD simulations of aerosol transport inside a restaurant showed a correlation between a high aerosol exposure index and reported infections, suggesting the use of shielding to control local flow patterns [22]. Eulerian–Lagrangian modeling of aerosol dispersion inside a music classroom found that using a portable air purifier close to the source was effective in reducing transmission [23]. Similar Eulerian–Lagrangian modeling of respiratory events in a public bus with central HVAC showed that particles greater than 200 µm were unaffected by the HVAC flow, while aerosols were significantly influenced by it. Schreck's study characterized a classroom setting using mathematical and numerical methods [25]. This study reported the sensitivity of aerosol dispersion to different classrooms, highlighting the importance of ventilation and the use of air purifiers. A similar study focused on transmission and mitigation strategies in a classroom setting and emphasized the effectiveness of combining face coverings and ventilation with air purifiers as the optimal approach for mitigation [26]. Likewise, the study examined the impact of human physiological factors in droplet dispersion from a sneeze and found that the nasal/buccal passage had significant effects on the spray characteristics which led to different transmission rates [27]. Overall, outdoor environments (with better ventilation, no spatial confinement, and increased distance between individuals) are generally more conducive to limiting COVID-19 transmission compared to indoor environments [23]. However, an LES simulation of two people talking inside a ventilated room showed the existence of the worst-case value of air changes per hour for scenarios with a small number of people and large distances between the occupants with respect to the size of the room [28].

The impact of passenger seating position inside a car on the driver's inhalation of infectious droplets was studied using an Eulerian–Eulerian model coupled with a k-ϵ turbulence model [29]. This simulation of human breathing and speech found that, within 6.38 min, a person inside a car can become infected with contaminated droplets due to the car's poor ventilation [29]. A similar approach was applied to a restaurant's indoor environment, revealing that it takes 10 min for a person sharing a table with an infected individual to become infected [30]. Likewise, the investigation extended to a scenario with a group of people standing inside a room, and found that a person directly facing an infected individual inhaled 1000 aerosol droplets within 30 min [31].

There are many studies associated with face coverings that aim to mitigate air-borne transmission [2,13,32,33]. Other strategies to reduce airborne transmission are social distancing, quarantining, and self-isolation, which were widely practiced during the SARS outbreak. This research focused on the concept that the flow of droplets and aerosols can be regulated by modifying the saliva droplet properties by consuming food particles like cornstarch, xanthum gum, lozenges, and Zingiber, which are called saliva modifiers hereafter. The primary experiment that examined the impact of the consumption of these food particles on saliva droplet properties was conducted by Reyes et al. [8]. The consumption of saliva modifiers has the ability to modify the size, viscosity, and flow rate of saliva droplets. The initial premise of this research was that increasing the droplet size with the use of a saliva modifier would aid in the efficient settling of droplets released during the respiratory process. The research preformed a critical analysis of the idea of enhancing the settling rate by increasing the saliva droplet size through the utilization of various saliva modifiers.

This paper is structured as follows. First, the computational fluid dynamics (CFD) model used to study the impact of modifying saliva fluid properties is described, including the model formulation, domain, computational mesh, and mesh sensitivity study. With confidence in the model, the study then moved to evaluate the impact of the flow velocity of the initial and final stages of a sneeze on the dispersion characteristics. Systematic studies of realistic modifications to saliva by varying the droplet distribution and/or viscosity using

saliva modifiers were performed and the aerosol reduction was compared with that of the base case scenario. The study then explored the connection between the saliva modifiers and droplet breakup morphology. The observed results are discussed with consideration of the various assumptions used in the study. Lastly, the conclusions drawn from the research are explained.

2. Methods

2.1. Computational Model Formulation

A commercial CFD code, Star-CCM+ [34], was used to investigate the links between saliva fluidic characteristics (viscosity and content/amount) and how they relate to transmission physics. Content refers to the total volume of saliva droplets that are created during a sneeze and relates to input particle distribution and the mass flow rate. The research utilized a CFD approach formulated with a Eulerian gas model, coupled to a Lagrangian droplet model, to track the dispersion of pathogens. The Eulerian model focuses on solving the velocity field from a turbulent puff associated with sneezes, which couples it to a multicomponent gas phase and a turbulence-resolving simulation. The Eulerian model equation sets are solved as 2nd-order equations that are accurate in both time and space, with implicit unsteady solvers employing the SIMPLEC algorithm. The liquid Lagrangian saliva droplets are coupled to this gaseous flow through an essentially one-way interaction driven by momentum coupling, and a weak two-way interaction associated with the coupling of the evaporation processes to the gaseous species [27]. A representative physical model for the cases investigated in this study is described in Figure 1, which aimed to represent an adult human within a ventilated room and was adapted from Ref. [27].

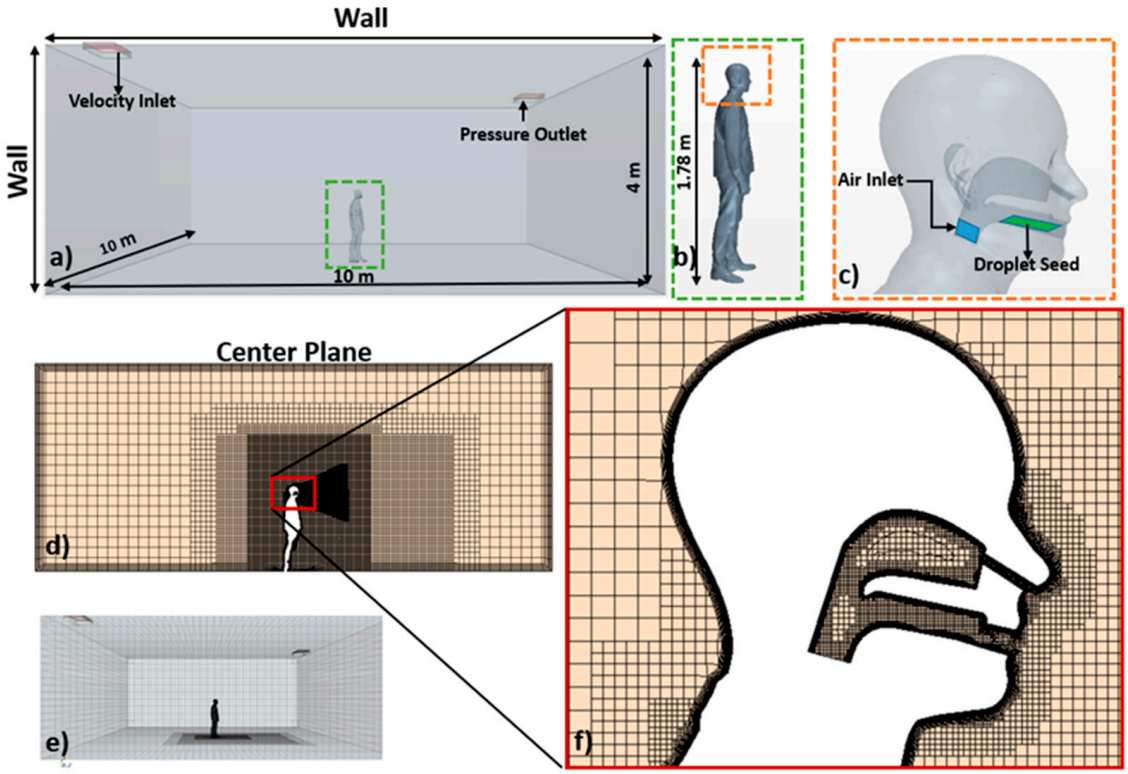

Figure 1. (**a**) Domain configuration schematic. (**b**) Human body model. (**c**) Air and droplet inlet in upper respiratory tract. (**d**) Discretization of domain. (**e**) Mesh sizes on center plane. (**f**) Refined mesh around the upper respiratory tract.

The computational domain depicts an adult with a height of 1.78 m positioned at the center of a 10 m $\times$ 10 m $\times$ 4 m room, as indicated in Figure 1a,b. The human model also includes an approximate upper respiratory tract (URT) that has buccal and nasal

cavities, as well as the top of the esophagus, as presented in Figure 1c. The computation mesh discretizing the domain is depicted in Figure 1d–f. The computational mesh is a hex-dominant, octree-based mesh with 12 prism-layer refinement of the wall's surfaces, which are associated with skin/clothes as well as the URT. Overall, the mesh has 3.3 million computational cells, with a maximum skew of 84.9°. In addition, the mesh has a refinement region in the exhaled puff region, as illustrated in Figure 1e,f, to resolve more scales of the resulting turbulence. Three different types of control volumes were used to refine the exhaled puff region, as can be observed in Figure 2. The conical, cubical, and rectangular control volumes used had the most refined meshing close to the mouth, with the least refined meshing away from mouth. The refinement of the computational mesh was relative to the base reference size and was 5% for conical, 15% for cubical, and 30% for rectangular control volumes. Altogether, 3.29 million cells constituted the computational domain. This model is the proposed approach for capturing the effect of sneezing within a room that was used to perform the sensitivity studies.

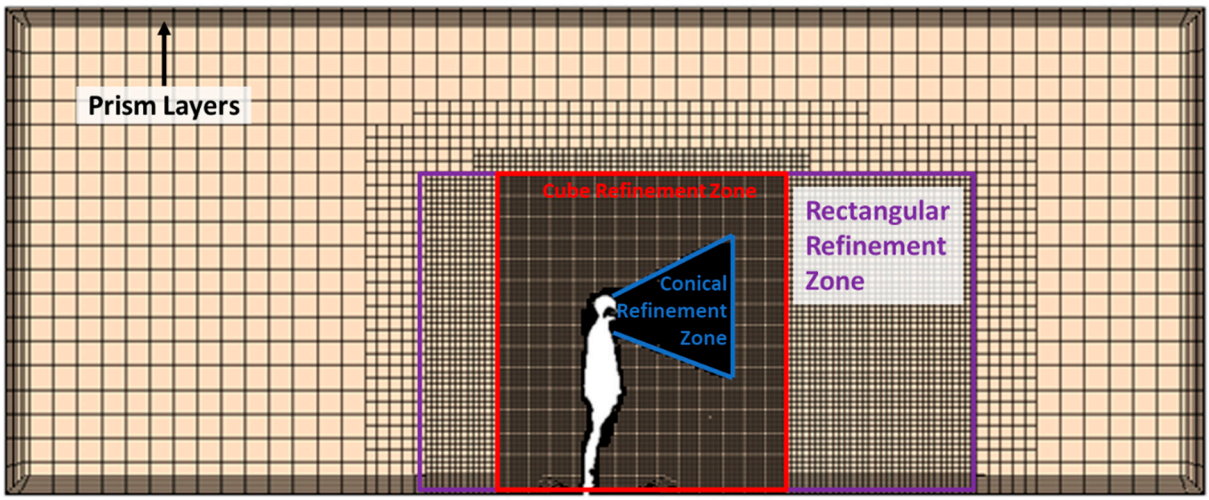

Figure 2. The control volumes used to refine meshing around flow-dominant regions.

In Figure 1c, air is injected into the bottom of the URT (blue area) using a variable velocity profile, as shown in Figure 3a [27]. Such a time-varying velocity was used to represent the time history of a human sneeze. Note that the velocity peaked at 48 m/s for the initial 1 ms, then decayed as a two-step decay. There was an initial exponential decay from 48 m/s to 2.5 m/s over 0.05 s. Thereafter, a linear decay was implemented using a velocity that approached 0 m/s after 0.5 s. This provides a physiologically reasonable human sneeze model [27]. Next, a baseline input droplet (particle)-size distribution (PSD), based on a bimodal, log-normal, Gaussian distribution [35], was utilized, as shown in Figure 3b, which was tied to the mass flow rate to count the number of droplets at the inlet mouth. The first distribution of the bimodal distribution had a mean $\mu_1 = 72$ µm and standard deviation $\sigma_1 = 1.5$. Likewise, the second distribution of the bimodal distribution had a mean $\mu_2 = 386.2$ µm and a standard deviation of $\sigma_2 = 1.8$. The combination of the input velocity and PSD are specific to a sneeze and provide a hypothetical case to study. The sneeze air jet interacts with the ambient conditions in the room and the initial temperature and pressure were set at standard conditions ($T = 25$ °C, $P_\infty = 101,325$ Pa). In order to create a realistic buoyancy-driven flow, realistic thermal boundary conditions were applied, with the room surfaces (walls/ground/floor) having a temperature of 23 °C and the human having a body temperature of 29 °C, buccal and breath temperatures of 37 °C, and a face temperature of 33 °C. There were also ventilation ports associated with the HVAC, shown in the top-left and top-right part of the room in Figure 1a, which circulate the flow at a constant velocity of 0.1 $\frac{\text{m}}{\text{s}}$ and the inlet temperature was 24 °C. This summarizes the model setup, and the overall model formulation is further discussed below.

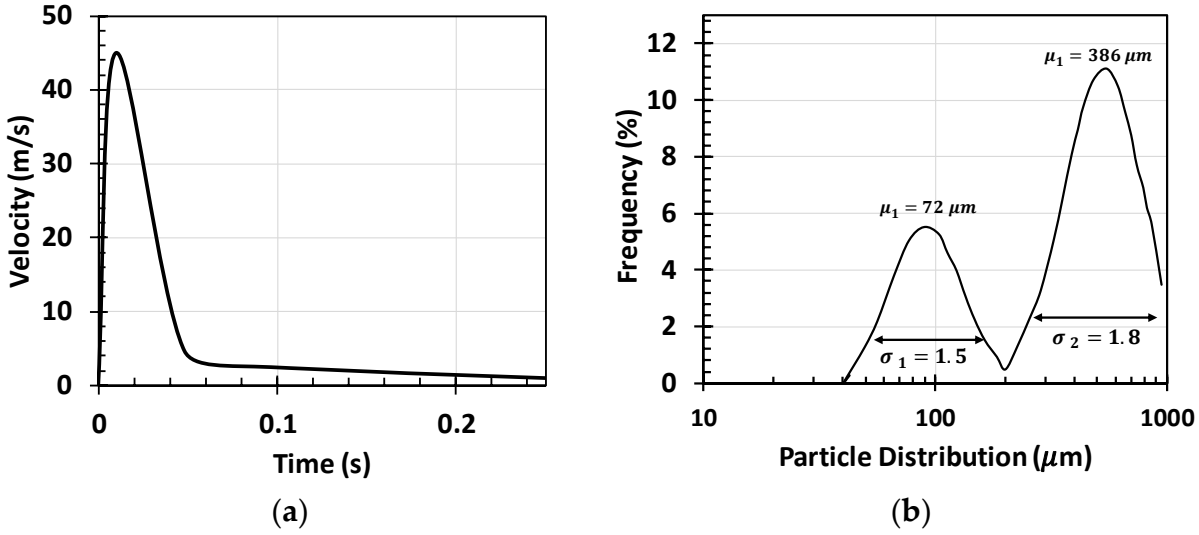

Figure 3. Input conditions relevant to the velocity and droplet size distribution. (**a**) Input velocity profile [27]. (**b**) Input droplet size distribution [35].

First, we will discuss the approach for modeling the gaseous flow using a Eulerian-based CFD model. Similar to Refs. [2,3,36], the gas phase was solved through Equations (3)–(6), which represent the mass, momentum, energy, and gas-species-concentration equations, respectively.

$$\frac{\partial \rho}{\partial t} + \nabla \cdot \left(\rho \vec{u} \right) = 0 \tag{3}$$

$$\frac{\partial \rho \vec{u}}{\partial t} + \nabla \cdot \left(\rho \vec{u} \otimes \vec{u} \right) = -\nabla \cdot pI + \rho \vec{g} + \nabla \cdot \bar{\bar{\tau}} \tag{4}$$

$$\frac{\partial (\rho E)}{\partial t} + \nabla \cdot \left(\rho E \vec{u} \right) = \nabla \cdot \left(k + \frac{C_p \mu_t}{Pr_t} \right) \nabla T + S_{e,evap} \tag{5}$$

$$\frac{\partial \rho Y_n}{\partial t} + \nabla \cdot \left(\rho \vec{u} Y_n \right) = \nabla \cdot \left(\rho D_n + \frac{\mu_t}{Sc_t} \right) \nabla Y_n + S_{Y,n,evap} \tag{6}$$

In the aforementioned equations, ρ is the gas phase density, E is the total energy per unit mass, I is the identity tensor, $\vec{u}$ is the velocity-vector field, p is the pressure field, $\bar{\bar{\tau}}$ is the shear stress tensor, μ_t is the turbulence viscosity, C_p is the specific heat capacity, k is the thermal conductivity, Y_n is the local mass fraction of species n, D_n is the diffusion coefficient for species n, Pr_t is the turbulent Prandtl number, and Sc_t is the turbulent Schmidt number, which is also used in Detached Eddy Simulation (DES) models [37,38]. Note that DES is a hybrid large-eddy simulation (LES) that simulates large-scale turbulent scales that the resolved mesh and time scales can support. The DES model then reverts to the underlying unsteady Reynolds-averaged Navier–Stokes (URANS) model based on Spalart and Allmaras where the spatial and temporal resolutions of eddies are not supported [39]. Additionally, the model employs a high Reynolds number wall treatment and ensures that appropriate values of y+ values in the range of 0–26 are used in the prism layers. Furthermore, it should be noted that this model is assumed to be incompressible but still includes thermal density variations through $\rho = \frac{P_o}{RT}$, where P_o represents a reference pressure and R and T are the ideal-gas constant and temperature, respectively. The system of equations is solved using a segregated SIMPLE-C-based algorithm with second-order numerical accuracy in both space and time.

The Lagrangian aspect of the model is utilized to track the droplet/aerosol/viral particle dispersion. The model accounts for aerodynamic drag [40], shear-induced lift, buoyancy, weight, pressure gradient forces, and liquid evaporation based on the Ranz–Marshall correlation [41]. The acceleration of droplets is determined by Newton's second

law considering the aerodynamic drag (F_{d_i}), lift (F_{l_i}), buoyancy/weight (F_{w,b_i}), and pressure gradient forces (F_{pi}), as illustrated in

$$m_d \frac{du_{d_i}}{dt} = F_{d_i} + F_{l_i} + F_{w,b_i} + F_{pi}, \tag{7}$$

$$\frac{dx_{d_i}}{dt} = u_{d_i}. \tag{8}$$

The droplet velocity vector $u_{d,i}$ has three velocity components indicated by the subscript i. The position is indicated by $x_{d,i}$ and m_d is the droplet mass.

The multicomponent droplet evaporation model assumes that the droplets have an internally homogeneous mixture of vaporizable water and inert components that do not undergo vaporization and represent residual products of dehydration (including viral particles). Such assumptions are important to consider as the overarching goal was to add compounds to saliva, which can alter such assumptions. Additionally, our work assumed that the droplets contain viral and solid debris that eventually become the aerosol. Hence, 10% of the mass was assumed to be non-evaporating, which was intended to represent the minerals as well as viral particles [42]. These droplets transported by the flow continuum reach a wall and become stuck on the wall. In general, the model supports two mechanisms that alter the size of the droplets during the sneeze: secondary droplet breakup and evaporation. Droplet breakup is based on the Taylor analogy breakup (TAB) droplet breakup model [43]. This secondary breakup mechanism is initiated by aerodynamic forces and is related to the *We* and *Oh*. The TAB model establishes an analogy between oscillating and distorting droplets within a uniform external flow field and a spring-mass system under forced and damped oscillations [44]. The restoring force of the spring, the external force on the mass, and the dampening are equivalent to the surface tension, aerodynamic force, and droplet viscosity, respectively [44]. Breakup in the TAB model occurs at the critical Weber number (We_{crit}), given as

$$2We_{crit} = \frac{C_k C_b}{C_F}. \tag{9}$$

Equation (9) is the constraint from the experiment that relates the dimensionless constants C_k, C_b, and C_F [44]. The onset of the bag breakup is determined by the critical Weber number (We_{crit}), which was estimated to be 5.5 ± 1 [43]. The TAB model also predicts the velocity of children droplets formed post-breakup in a path perpendicular to the parent-droplet trajectory [44]. These secondary breakup processes are important as they generate a large number of small droplets, resulting in an increased surface area-to-volume ratio that enhances mass transfer (evaporation) and aerodynamic drag (decreases settling).

The second physical model relating to the droplet size evolution relates to evaporation. The rate of mass change of the droplet due to a quasi-steady evaporation is described by

$$\dot{m} = -g^* A_s l(1 + B)\ . \tag{10}$$

The model is simplified here and additional details are provided in Ref. [34]. In Equation (10), B is the Spalding transfer number, A_s is the droplet surface area, and g^* is the mass transfer conductance (in the limit $B \to 0$) provided by the Sherwood number (Sh) that is computed using the Ranz–Marshall correlation, which is defined as

$$Sh = 2 + 0.6Re^{1/2}Sc^{1/3}, \tag{11}$$

where Re is the phase pair Reynolds number and Sc is the Schmidt number calculated as

$$Sc = \frac{\mu}{\rho D}, \tag{12}$$

where D is the species diffusivity within a phase. Such a model also accommodates relative humidity changes associated with changes in the ambient water vapor content.

2.1.1. Model Summary

In the model, of the flow is characterized being both continuous and incompressible, aspects that align with conventional models for sneezing and breathing. The flow is likely to be somewhat turbulent, although it might also be in a transitional phase between laminar and fully developed turbulence. Given that human respiratory fluids behave as Newtonian fluids, their viscosity remains constant regardless of the flow conditions. The model assumes gaseous species and characteristics that are associated with inhaling and exhaling, requiring second-order considerations to accurately capture the complex interactions and the exhaled breath is treated as an ideal gas to simplify the calculations. However, the most significant factors contributing to uncertainty in these models stem from the variations between individuals, such as differences in sneezing force, respiratory tract anatomy, and fluid properties, which were not accounted for in a standardized way. These human-to-human variations pose a substantial challenge to accurately predicting and controlling the airborne transmission of pathogens. One limitation is that the study focused on simplified scenarios, while real scenarios are much more complex. Table 1 provides a summary of the CFD model characteristics. Such model attributes are expected to provide sufficient insight into this particular type of respiratory event.

Table 1. The summary of the computational characteristics of the model.

Model	Value/Option	Comments
Turbulence	Spalart–Allmaras DES	Fully turbulent, all-y^+ wall model, implicit, unsteady
Solver	Segregated flow	Segregated in terms of flow, species, and energy
Time Stepping	Adaptive time stepping	The minimum time step of 1×10^{-5} s accounts for the exponential flow of sneezing at the beginning
Meshing	Hex dominant with prism layers	Hex dominant with 12 prism layers around the wall, body wall, and URT

2.1.2. Approach to Assessing Saliva Modifiers

As the objective was to observe the impact of modifying saliva by incorporating (edible/safe) compounds such as cornstarch, xanthum gum, lozenges, and Zingiber officinale, the initial conditions for the droplets emitted during the sneeze phenomenon through these variations are critical. This is perhaps the most uncertain aspect of this study, but to estimate their effects, experimental measurements of viscosity of human saliva after eating the various ingredients were obtained from Ref. [8] and utilized in this study. In that study, saliva modifiers were found to influence the fluid properties of saliva in terms of the viscosity and mass flow rate of saliva produced in the mouth. Lastly, some experimental observations during sneezes also indicated that the mean droplet size was affected. Using a best-estimate approach after analyzing those data, the input characteristics were adjusted, as summarized in Table 2. Xanthum gum and cornstarch behave like colloids and create microscopic forces that alter the viscosity. Zingiber has the biological effect of mitigating saliva generation within the mouth and, hence, does not stimulate saliva. Lozenges do stimulate saliva. In general, cornstarch led to almost 50% larger droplets, increased the viscosity slightly, and did not affect the content. Xanthum gum increased the droplet size by 25% while significantly increasing the saliva viscosity. The lozenge increased the droplet size by 50% and slightly increased the viscosity, while significantly (over 100%) increasing the saliva content. Lastly, Zingiber reduced the droplet size, did not affect saliva viscosity, and decreased the content by about 70%. Using these data, the experimental

parameters of the input droplets were modified. Hence, the model accommodates primary break-up and fluid-property alterations through the use of experimental observations. Such a process enables an assessment of the consequences of these saliva modifiers on airborne viral transmission.

Table 2. Estimated impact of foods on droplet characteristics observed in human sneeze experiments [8].

S.N.	Saliva Modifier	Mean Droplet Size (Relative to Base Size)	Viscosity (10^{-3} Pa·s)	Mass Flow Rate (10^{-5} $\frac{kg}{s}$)
1	Base Case (Saliva)	1	1.36	1.07
2	Cornstarch	1.5	1.43	1.07
3	Xanthum Gum	1.25	28.94	1.07
4	Sugar-Based Lozenge	1.5	1.79	2.28
5	Zingiber officinale	0.5	1.36	0.215

2.2. Comparison with Experiment

In order to compare our sneeze model results with experimental observations, the simulation results were qualitatively evaluated against an image from a human sneeze experimental study [42]. There was no strong correlation between the inputs; therefore, such a comparison was intended to compare the characteristic shape and general characteristics. In Figure 4, the CFD result at 0.1 s was compared with a photograph from an observed sneeze [42] at 0.1 s. In the CFD model, the droplets traveled further at 0.1 s; it can be conjectured that the model used a higher velocity than the sneeze event. Hence, our CFD model likely used a more intense sneeze than the one in the experiment. It is critical to recall that a human sneeze is highly variable, and therefore, a stronger sneeze is reasonable. To make use of this comparison, consider the angle that captures the extent of the puff, Θ. A value of Θ from the CFD model is indicated in Figure 4b and was observed to be roughly 106°. This same angle was positioned on the image from the experiment and indicates a close correlation between the initial puff dispersion rates. Hence, the overall initial expansion of the droplets from the CFD model did appear to compare well with the experimental observations, specifically with respect to the rapid initial expansion of the droplets. In the context of a highly variable event such as a sneeze, the CFD sneeze model compared well and appeared to reasonably replicate a real human sneeze event to the degree necessary to perform sensitivity studies.

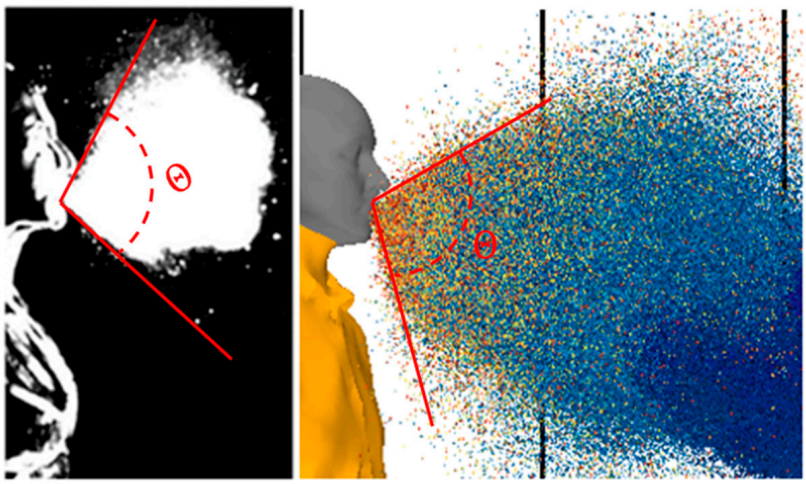

(**a**) (**b**)

Figure 4. Comparison of the droplets released from the CFD model and experiment at roughly 0.1 s after the sneeze. (**a**) Experiment [42]. (**b**) CFD.

2.3. Mesh Sensitivity Study

A mesh sensitivity study was conducted to provide numerical simulations independent of the mesh refinement. Three grid levels were simulated using a reference grid size of 0.5 m, which was the reference dimension for all mesh settings. The mesh was then systematically refined by reducing the parameter to 0.2 m (medium), with a total cell count of 3.3 million, and 0.1 m (fine), with a total cell count of 20 million. The maximum CO_2 extent reported up to the time point of 0.2 s was used to evaluate the mesh sensitivity. The results are plotted in Figure 5b as a plot of the maximum extent (y-axis) as a function of time and indicated that the CFD results were within the asymptotic range of convergence with a relative mesh size of 0.2 m. As can be observed in Figure 5b, the temporal trend from coarse (0.5 m) to fine (0.1 m) meshes approached the fine mesh (0.1 m) and indicated an asymptotic convergence. Based on such an observation, the study moved forward with a relative mesh size of 0.2 m. Figure 5a shows the iso-surface of the maximum CO_2 extent at 0.2 s for the three relative mesh sizes mentioned before to visually see the impact. Here, it can be observed that the medium (0.2 m) and fine (0.1 m) grid cases had similar iso-surfaces for CO_2 compared to the coarse mesh of 0.5 m, further indicating that the 0.2 m mesh is a reasonable grid. Considering the unsteady and turbulent nature of the flow, achieving an asymptotic range of mesh is unlikely and computationally expensive. Hence, this study moved forward with a 0.2 m mesh consisting of 3.3 million cells for further analysis. The cases were run on the UCF's Newton computational cluster. Each case was run on each node, where each node has 1 GB RAM and 48 cores, and is powered by Intel Xeon 64-bit CPUs. Each case roughly took 8064 CPU hours to model 5 s of the sneeze.

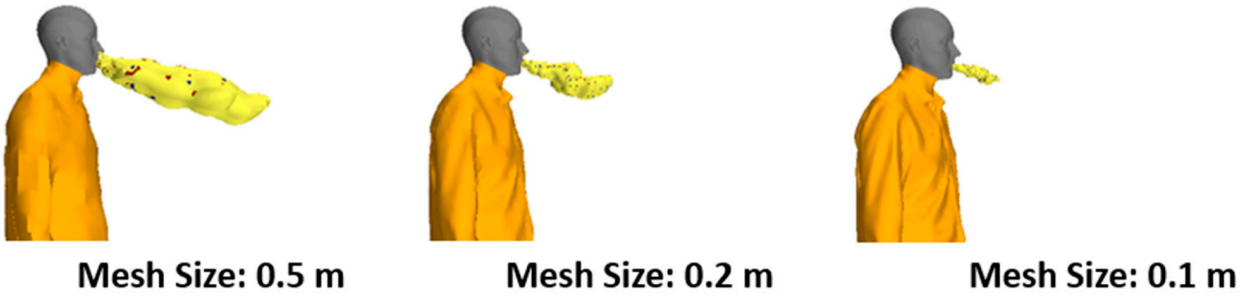

(**a**) Iso-surface at 0.2 s for various mesh sizes

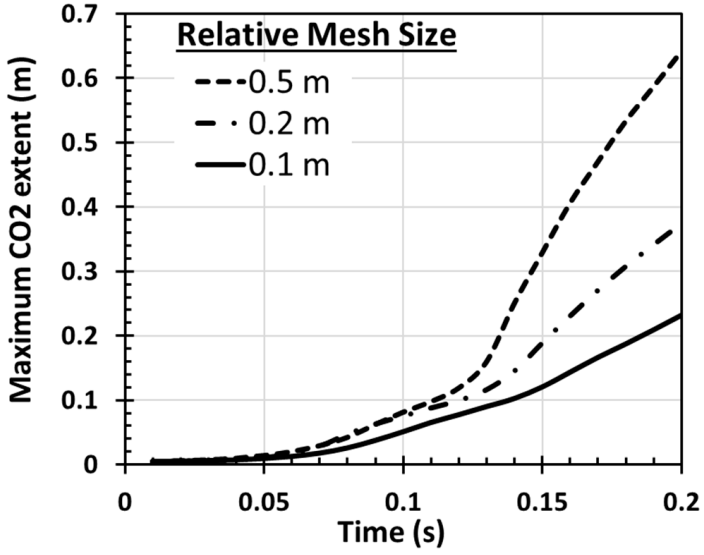

(**b**) Maximum extent over time

Figure 5. CO_2 extent for different relative mesh sizes.

3. Results

3.1. Dispersive Velocity Characteristic

As most of the dispersion depends on the underlying velocity, the velocity field was first evaluated. Note that this velocity field was essentially fixed for all the variations. Figure 6 shows contour plots of the velocity magnitude through a plane through the center of the mouth. The contour plots show several time intervals throughout the sneeze event from 0.1 to 5 s. Figure 6a shows the progression of the more intense, early phase of the sneeze, occurring from 0.1 s to 0.5 s. During this initial stage, a conical shape emanating from the mouth was apparent. Over time, this shape grew in size and diminished in velocity magnitude. At 0.1 s, the maximum velocity magnitude reached 8.3 m/s, gradually decreasing to 1.4 m/s by 0.5 s. It is worth noting that the highest velocity tended to be concentrated at the forefront of the burst. Within the conical shape, turbulent eddies were evident, extending up to a distance of 0.762 m (2.5 ft), while the plume steadily expanded as the cone widened, reaching up to 1.07 m (3.5 ft). In Figure 6b, the long-term effects (from 1 s to 5 s) can be observed. In this figure, it can be seen that the velocity magnitude continued to diminish, from a maximum of 0.9 m/s to 0.3 m/s, and the cone shape of the velocity plume continued to grow in volume. After 5 s, the plume had traveled a distance of up to 1.83 m (6 ft). Additionally, there was an apparent presence of turbulent eddies that persisted and had the ability to dominate the long-term dispersion characteristics.

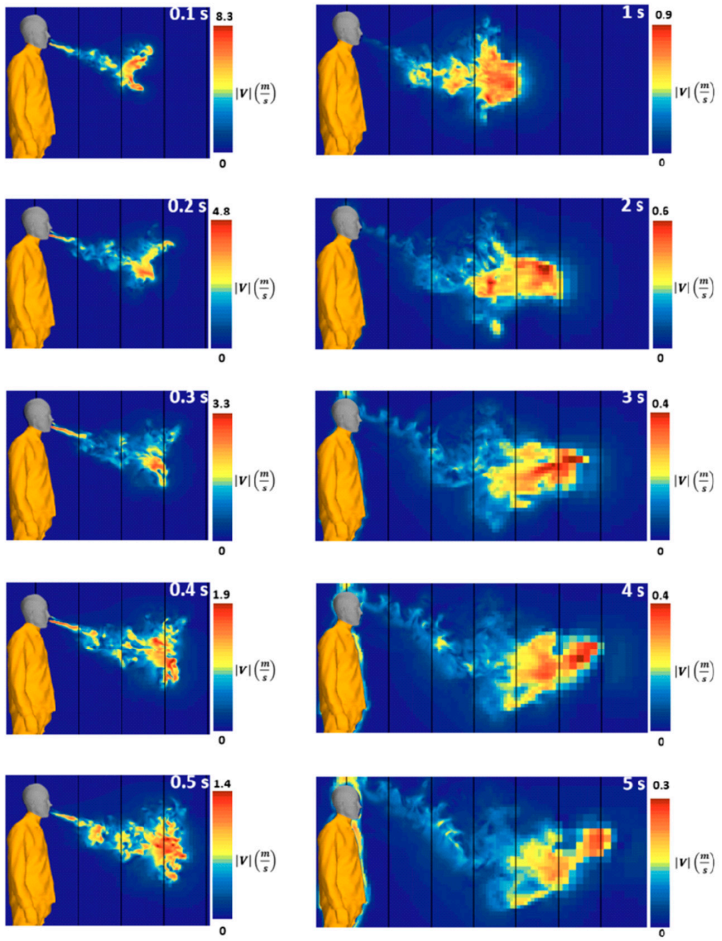

(**a**) Initial development of plume (**b**) Later stage of sneeze

Figure 6. The temporal velocity contour of sneeze. (**a**) Velocity contour of early stage of sneeze showing the development of plume. (**b**) Velocity contour of a later stage of sneeze. Note that two adjacent vertical lines indicate a 1 ft distance.

3.2. Dispersion Due to Turbulence

Sneezing is a vigorous respiratory event with a flow of speed as high as 50 m/s, which generates turbulence eddies. The Reynolds number at the mouth (Re_m) was defined as

$$Re_m = \rho V_m D_m / \mu, \tag{13}$$

where V_m is the maximum velocity of flow at the mouth, which was 48 m/s; the density of air ρ was 1.225 kg/m^3; the diameter of the mouth D_m was 0.015 m; and the kinematic viscosity of air (μ) was $1.81 * 10^{-5}$ Pa·s. This resulted in a maximum Reynolds number of 48,761, which is greater than the critical Reynolds number of 40,000, suggesting that the flow will be fully turbulent if it fully develops. The turbulent nature of flow is characterized by the presence of turbulence eddies. Droplets are trapped inside turbulence eddies, which overturn the flow of droplets opposite to the direction of gravity, prolonging the settling of droplets. Eddies are formed due to turbulence during sneezing, which can be represented as the iso-surface of the Q-criterion, as shown in Figure 7. The eddies and particles are colored according to their velocity magnitude and the size of the droplets, respectively. By 5 s, the magnitude of the maximum velocity of the eddies was already reduced to 0.3 m/s. The figure shows that most of the droplets smaller than 100 µm were influence by turbulence eddies, trapping these droplets inside the eddies and increasing the airborne time of the droplets. The larger particles (greater than 100 µm) were minimally affected by such turbulences and settled by 5 s.

Figure 7. Turbulence eddies formed due to sneezing at 5 s.

3.3. Early-Stage Dispersion and Impact of Saliva Modifiers

In the context of the previously mentioned flow field, the dispersion of saliva was evaluated further. This also included studies of the impact of the modifiers. In this section, the studies looked at the early and late stages of the sneeze. The study on the early stage focused on droplet break-up, while the study on the late stage focused on dispersion. In general, efforts were made to understand how the saliva modifiers affect the initial PSD and TAB breakup during these stages.

Figure 8 shows plots of the initial droplet dispersion during the early stage of the sneeze. This plot shows the initial droplet dispersion from 0.1 s to 0.5 s, with the 0.1 s time point in the first row, and each row shows the subsequent time point until the last row, which is the 0.5 s time point. Each column presents the variation in the saliva. The first column is the baseline case, while the subsequent columns represent the cases where the saliva was mixed with cornstarch, xanthum gum, a lozenge, and Zingiber. In this plot, the particles are colored based on the droplet size. Hence, Figure 8 collectively visualizes the impact of the saliva modifiers on the early stages of dispersion.

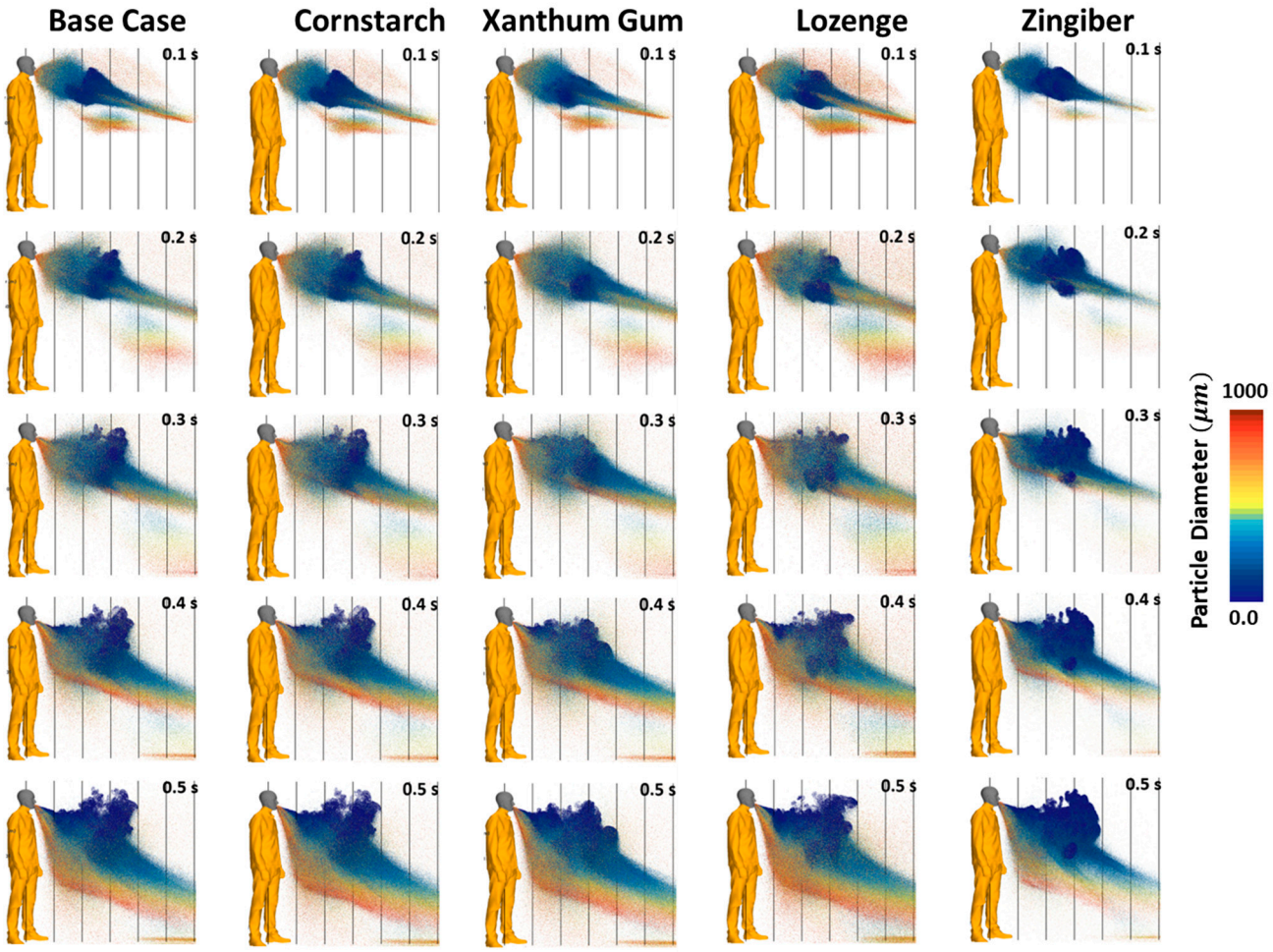

Figure 8. Droplet particles released during early stage of sneezing from 0.1 s to 0.5 s for all cases. Note that the vertical lines indicate 0.305 m (1 ft) intervals from the mouth.

We compared the effects of each modifier over time. At 0.1 s, all the cases displayed a clear trend of the droplets following the core of the plume, as indicated in Figure 6. In general, the larger particles (red) appeared to dominate the front of the plume, which was consistent for all the cases. At the right side of each case, the large droplets immediately traveled up to 1.82 m (6 ft). The larger particles also dominated the droplets that fell out of the plume. The smaller particles tended to concentrate around the center of the plume and appeared to be nearly the same in all the cases. The mid-sized droplets, however, displayed some variation between the cases. These droplets tended to dominate the upper, initially dispersed, regions of the plume. For the lozenge case, which was characterized as having an increased saliva content, the upper region of the plume had more droplets compared with the baseline, cornstarch, and xanthum gum cases. In this same region, the Zingiber case displayed an observable decrease in content. As time advanced, this initial trend persisted. Specifically, at t = 0.3 s, the Zingiber case showed a turbulent dispersion dominating the small droplets, which was covered by the presence of mid-sized droplets in the other cases. At 0.5 s, the initial front of the larger red particles moved out of the observed region. Additionally, the larger particles appeared to have settled out due to gravity. The smaller droplets appeared to persist due to their low terminal velocity, interactions with turbulent eddies, and suspension due to buoyancy-driven flows. These smaller droplets did not show a significant difference and demand further evaluations over longer periods.

3.4. Late-Stage Dispersion and Impact of Saliva Modifiers

Figure 9 highlights the long-term dispersion of droplets expelled during a sneeze under a variety of saliva conditions (indicated by each column), progressing in time from 1 to 5 s. The columns are similar to those in Figure 8 and represent the baseline, cornstarch, xanthum gum, lozenge, and Zingiber cases, respectively. In these plots, the droplets were accentuated to highlight the characteristics. As expected, the general trends observed appeared to indicate that the saliva changes (the droplet size distribution and droplet responses) were due to competing mechanisms.

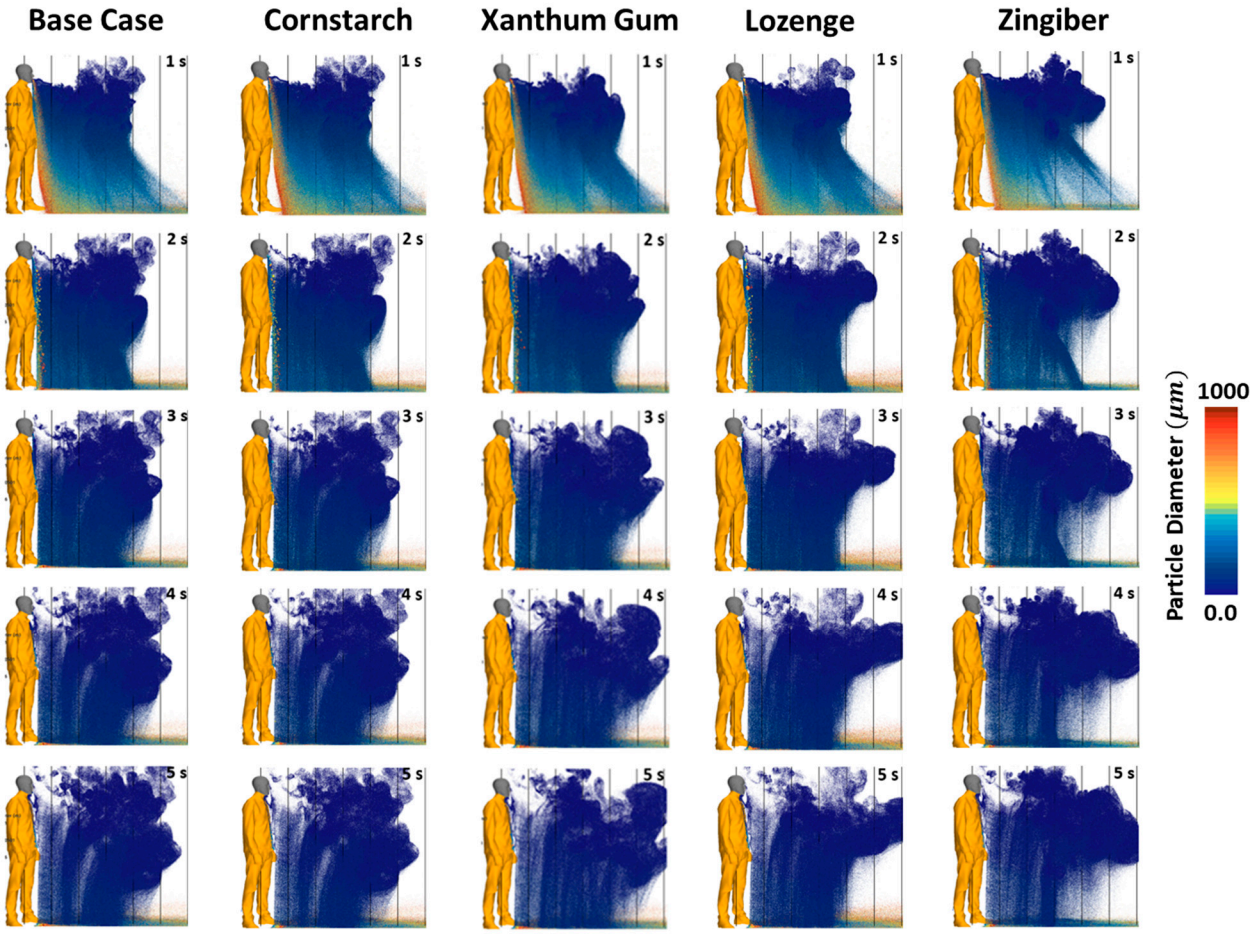

Figure 9. Droplet particles released during later phase of sneezing from 1 s to 5 s for all cases.

At the 1 s time point, in all the cases, the larger droplets (red) showed strong settling, the medium-sized (yellow) droplets were starting to settle, and the aerosols (blue) remained suspended. Comparing the various results, there were turbulent eddies cycling the aerosols upward and out of the plume in all cases except for the xanthum gum case. This can be attributed to the overall larger droplets formed in the xanthum gum case, which are less susceptible to turbulent eddies. In the Zingiber case, with a reduced mean droplet size, the aerosols appeared to travel further, by nearly 0.305 m (1 ft). Hence, at 1 s, much of the processes associated with settling and aerosol dispersion had already started.

In the remaining time, a clear separation of scales emerged. At 2–3 s (in rows 2–3), the large and medium particles had mostly settled out and the aerosols persisted. It is important to recall that the aerosols are exaggerated in size; hence, these plots must be interpreted as trends and not the actual content. At 4 s, only the aerosols remained suspended. It is noticeable that the turbulent eddies tended to trap these aerosols and disperse them vertically upward, which was most prevalent for the lozenge case, followed by the cornstarch and baseline cases. The lozenge, xanthum gum, and Zingiber cases showed a range of smaller

particles that reached the 6 ft (~3 m) mark earlier than the baseline and cornstarch cases, which occurred during the 2–3 s time period. At 4 s and beyond, these cases showed dispersion well beyond 6 ft (3 m). Additionally, after 4 s, only the aerosols remained suspended, and the flow appeared to be characterized by gradual settling and trapping within the residual turbulence within the puff. In general, the late-stage impacts of the saliva modifiers were some minor impacts on distance but the other characteristics were relatively similar.

3.5. Evaluation of Saliva Modifiers on Transmission Probability

In order to better quantify the impact of the saliva modifiers, we compared the droplet-size histograms at 5 s (provided in Figure 10). The overall particle count in the domain for the various size ranges and different saliva conditions (indicated by each bar) was plotted for droplets with a diameter smaller than 100 μm. Figure 10 shows how the saliva modifiers reduced the aerosols that drive airborne transmission. It was found that the cornstarch and lozenge reduced the initial droplet content for droplets up to 30 μm in size. On the other hand, Zingiber, which reduced the content and mean droplet size, increased the long-term count for these smaller droplets (<30 μm). For particles with sizes ranging from 50 to 100 μm, the cornstarch and lozenge were found to increase the droplet content. Alternatively, Zingiber reduced the amount of the particles with sizes in the range of 50–100 μm. The xanthum gum reduced the production of droplets with sizes ranging from 1 to 90 μm. However, the input particle distribution varied for each saliva modifier.

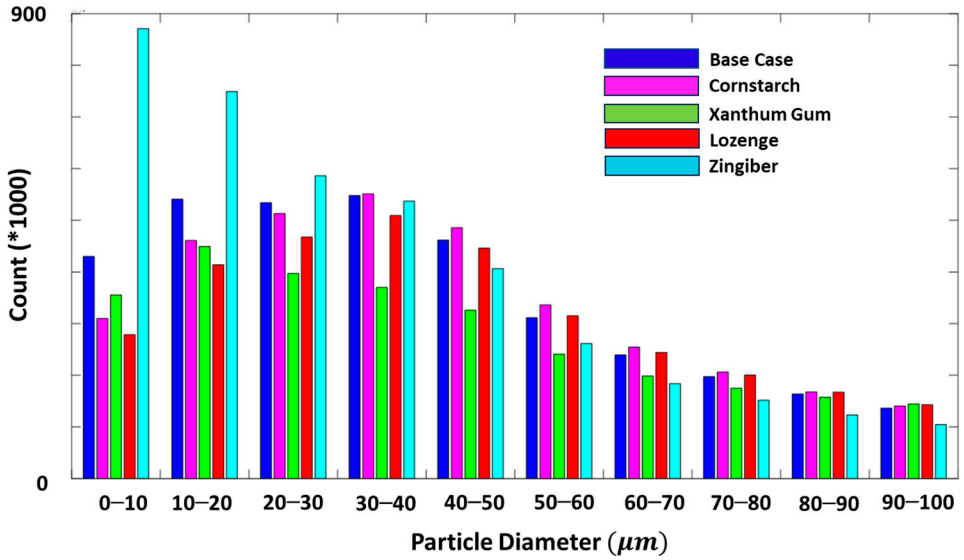

Figure 10. Histogram of particle distribution with saliva modifiers at 5 s after sneeze.

To better understand the mechanisms of the saliva modifiers, the overall droplet count at 5 s was normalized by the input count. The results from this are plotted and compared in Figure 11 for the various saliva modifiers. This plot reveals a couple of effects of the modifiers and highlights the aerosolization process. First, for the lozenge, cornstarch, and base cases, there was a noticeable peak at around 45 μm. This peak tended to be around 1.7–2 times the input value and is likely to be the result of a migration of the μ_1 input peak to lower diameters as those droplets are exposed to evaporation. A similar peak was observed for the Zingiber case; however, it was noticeably lower (~1.5), which was likely a result of the smaller input size distribution. Lastly, the case with the more viscous xanthum gum did not display this peak. Another observable trend was that the lozenge, cornstarch, and base cases all had similar trends throughout. In the xanthum gum case, there was a noticeable rise in aerosols. The most significant factor in this was probably change in the viscosity, which directly affects droplet breakup processes. Additionally, the Zingiber

case displayed a similar overall shape, but there was a noticeable drop in the initial and final droplet counts. The most notable change in the Zingiber case was the saliva content, which may indicate a scenario where the initial aerosols were more dominant. In any case, these plots indicate that the ratio of initial-to-final aerosols appeared to be higher when the viscosity and initial count are higher; this effect demands further interrogation.

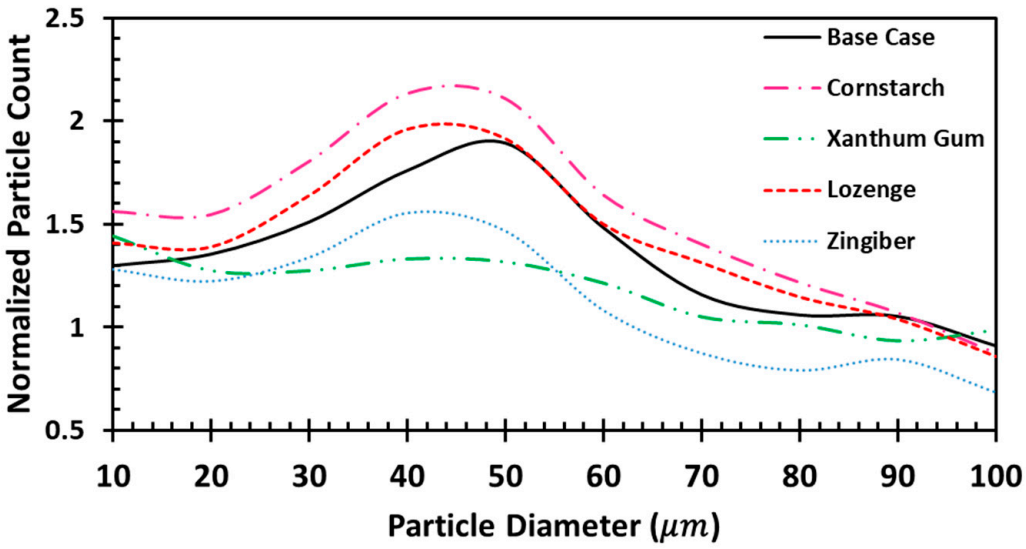

Figure 11. Count ratio of particles with different sizes at 5 s after sneeze compared to initial input with use of saliva modifier.

The total volume of the droplets expelled into the environment with the different saliva modifiers is shown in Figure 12a. In Figure 12a, the effect of each modifier on the volume expelled is indicated. The reader is reminded that these results are based on the rates of salivation from experiments [8]. The total suspended droplets (i.e., droplets at elevations of 0.1 m over the floor level) are shown in Figure 12b. The blue bars provide the amount of volume of liquid suspended, while the orange bars indicate the loss of liquid due to evaporation. Under the assumption that viral particles have a consistent concentration, the height of the orange bar provides an indicator of the increased viral load in the room from the sneeze event. Hence, the difference in values between Figure 12a,b is an indicator of the reduction in the viral load. The best case is indicated by the lowest amount of viral load, which was the xanthum gum case. This was a direct result of the increase in droplet size, which increases the probability that the droplets will fall to the ground. To better understand the trends, we plotted two ratios in Figure 12c. The first is the ratio of suspended droplet volume to input volume (Droplet Volume Reduction Ratio), which is an indicator of the reduction in saliva volume. Again, this metric is skewed as evaporation unfairly reduces it. Hence, we used the Viral Particle Reduction Ratio (orange bars) as a metric for the efficacy of the reduction relative to emission. Here, we can see that in the baseline case, roughly 53% of the viral particles were expelled. In comparison, in the cornstarch, lozenge, xanthum gum, and Zingiber cases, 35%, 29%, 21%, and 96% were expelled, respectively. The reduction with Zingiber was the largest due to the smaller droplets and increased propensity to evaporate. However, as seen in Figure 12b, there was still a reduction in the overall viral load. The most effective saliva modifier from these analyses was xanthum gum, which produced the largest reduction in viral load emission (Figure 12c) and had the lowest overall emission (Figure 12b). Overall, these analyses provide additional insights that suggest that xanthum gum has strong potential; however, this is somewhat inconsistent with the previous findings in Ref. [8], which suggests that additional studies may be required.

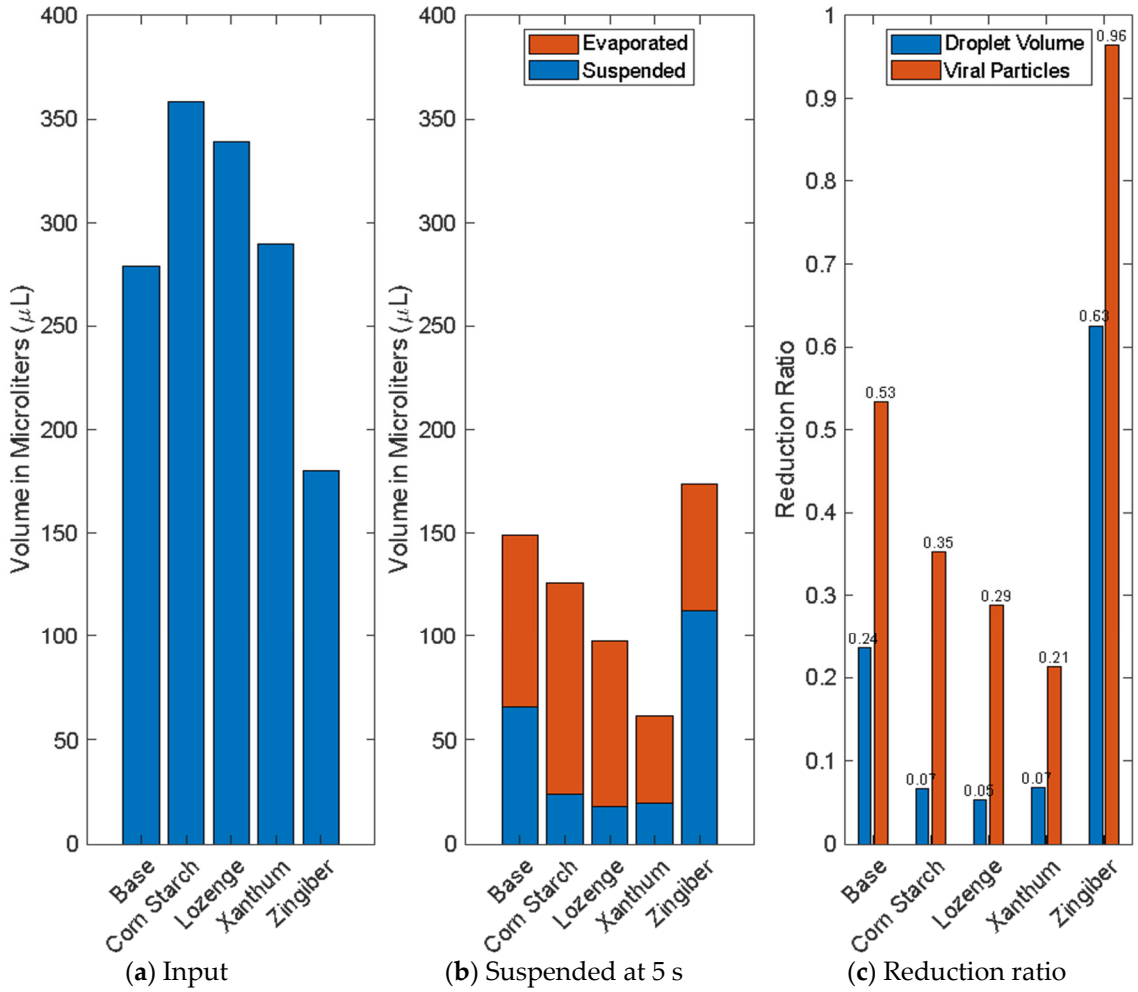

(**a**) Input (**b**) Suspended at 5 s (**c**) Reduction ratio

Figure 12. Bar charts depicting volume of droplets from a human sneeze. Part (**a**) represents the total volume for each case expelled into the environment. Part (**b**) represents the suspended droplets. Part (**c**) provides the reduction, i.e., final volume and viral particles divided by the input. Note that the suspended liquid volume is blue and the evaporated amount is indicated in orange.

4. Discussion

In order to better understand the results, the secondary droplet-breakup morphology was studied during the most intense time in the sneeze (at 0.02 s). Figure 13 shows scatter plots of the state of all the droplets at 0.02 s, plotted in terms of their instantaneous *We* and *Oh* states. The secondary breakup probability and morphology are highlighted using the conventional regime map which was overlaid on the plots. These plots are individual comparisons of the baseline to the cornstarch, lozenge, xanthum gum, and Zingiber cases.

The increase in the initial mean droplet size for the cornstarch, lozenge, and xanthum gum cases was expected to increase the Weber number and thus the likelihood of droplet breakup. In Figure 13, the cornstarch and lozenge cases appear to have the most droplets within the shear breakup and bag breakup regions compared to the base case scenario. This is likely the cause of the elevated aerosol counts in Figure 11 for those cases. In contrast, the xanthum gum case had an increase in the *Oh* for the bulk of the droplets, which was associated with the sharp rise in viscosity. Consequently, there was an expectation that the occurrence of bag breakup and shear breakup will be reduced. Returning to Figure 11, the combined result suggested that the lack of a hump (which is apparent in the other cases) was due to the saliva viscosity. Hence, the production of thicker saliva and larger saliva droplets appears to make the droplets more resistant to secondary breakup. Such a characteristic of droplets has been observed in experiments investigating the effect of

viscosity on the breakup phenomenon [45]. An increase in viscosity results in a higher Sauter mean diameter (SMD), defined as the diameter of a droplet that has the same volume-to-surface area ratio as all droplets in a spray combined. The reduced occurrence of breakup leads to a lower production of droplets, which decreases the overall surface area and consequently raises the SMD [45]. The Zingiber case (which initially developed smaller and fewer droplets) had a smaller range of *We* and *Oh* values compared to the baseline case. This also indicates that there was less exposure to the bag and shear-breakup modes. Such a shift is favorable and likely results in a smaller rise in the smaller droplets, as observed in Figure 11. Consequently, the Zingiber case exhibited a reduced breakup phenomenon due to the smaller initial droplets.

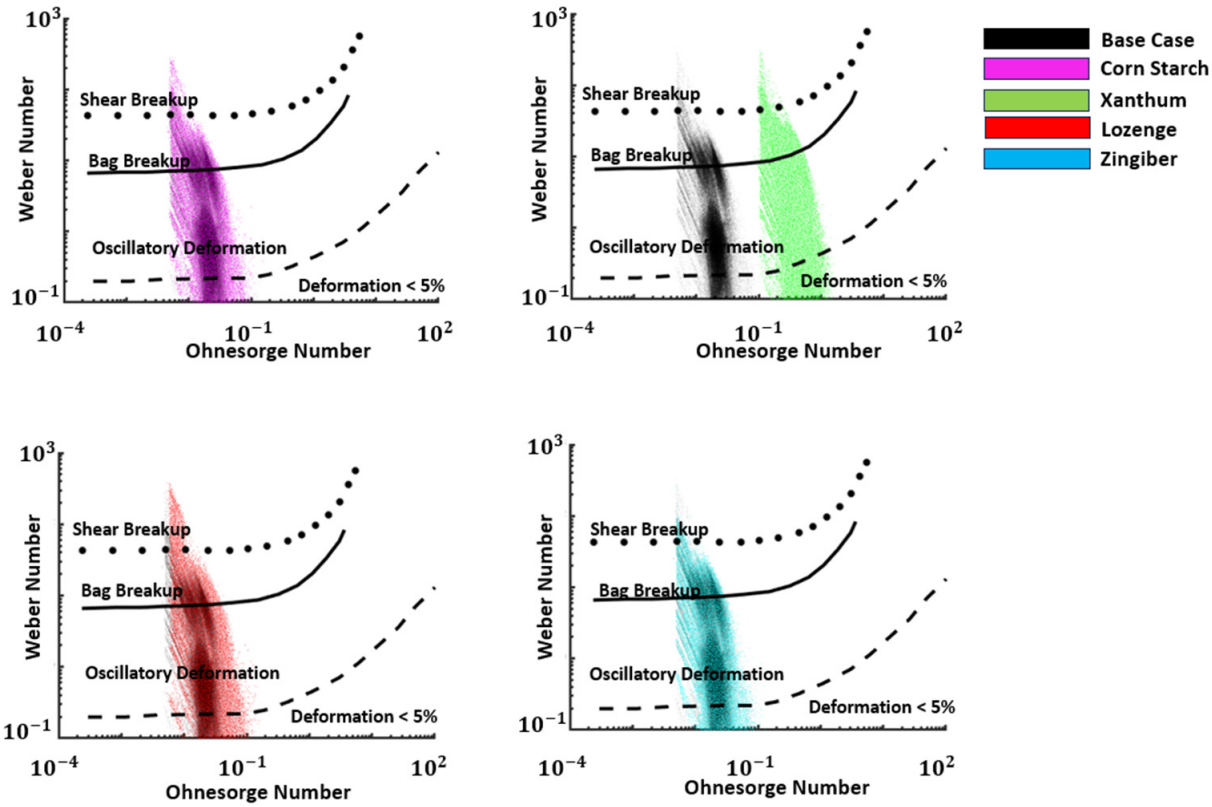

Figure 13. *We* vs. *Oh* of droplets at 0.02 s after sneeze with the use of saliva modifiers compared to the base case scenario.

In previous studies, several impacts on airborne transmission through modifying the saliva have been observed. Although the flow dynamics of the respiratory phenomenon are not influenced by these modifications, the resulting dispersion processes appear to correlate with parameters such as viscosity, mass flow rate, and initial droplet size due to the primary break-up mechanisms. Our findings suggest that some saliva modifiers such as cornstarch and sugar-based lozenges slightly increase the droplet size, yet do not reduce the settling time. In fact, these modifiers impede the settling of droplets due to the increased likelihood of vigorous breakup, leading to the formation of numerous secondary droplets. On the other hand, xanthum gum, which increases the droplet size at the mouth while also significantly increasing the viscosity by 2000%, was shown to be effective in producing droplets that are more likely to settle. Lastly, the Zingiber case had an increased amount of aerosols compared to the other cases, but relative to the initial amount, it was notably less. Overall, the results indicate that such parameters could be utilized to design and tune one's saliva to alter its transmission characteristics.

5. Conclusions

In this study, a Eulerian–Lagrangian hybrid CFD model was used to explore the sneeze respiratory phenomenon and the influence of saliva modifiers on droplet breakup. The goal was to understand how these modifiers can potentially affect airborne transmission with a specific focus on the initial droplet size distribution, saliva content, and viscosity. In this study, we observed that the saliva modifiers can affect the airborne transmission probability by altering both the initial droplet size and mitigating (from a probabilistic standpoint) secondary breakup. These results were based on initial droplet size distributions that were based on limited data; hence, there is a strong need to provide more experimental data to better understand these phenomena. Despite this limitation, the CFD model was able to uncover clear insights, especially the importance of secondary droplet breakup. Specifically, xanthum gum (with a 2000× viscosity increase) nearly eliminated the secondary breakup mechanism that dominates the aerosol formation process.

When evaluating the effectiveness of the saliva modifiers in reducing the overall droplet volume at the end the sneeze, the saliva modifiers that increased the mean droplet size proved to be effective. Cornstarch, xanthum gum, and the lozenge increased the mean droplet size by 50%, 25%, and 50%, respectively, leading to a reduction of 71.6%, 71.2%, and 77.2%, respectively, in the overall droplet volume compared to the base case scenario. However, the impact of the saliva modifiers was different when focusing specifically on the volume of droplets with sizes up to 100 μm compared to their effect on the overall droplet volume at the end of the sneeze.

The scope of the study can be extended to include the respiratory phenomenon of speaking and coughing. It is important to note that the effects of saliva modification may vary for speaking and coughing, which occur at a significantly lower flow momentum. The maximum flow speed for speech is around 6 m/s and for cough, it is around 20 m/s. The lower flow momentum during speaking and coughing can give rise to different breakup phenomena compared to sneezing. Consequently, the use of cornstarch and lozenges, which were ineffective in reducing the settling of saliva droplets, may yield contrasting results for speech and coughing phenomena. Furthermore, the research can be extended by using an additional range of saliva modifiers.

Author Contributions: Conceptualization, R.S. and M.K.; methodology, R.S. and D.F.; validation, R.S., D.F. and M.K.; formal analysis, R.S.; writing—original draft preparation, R.S.; writing—review and editing, D.F. and M.K.; visualization, R.S.; supervision, M.K.; project administration, M.K.; funding acquisition, M.K. All authors have read and agreed to the published version of the manuscript.

Funding: This research was funded by National Science Foundation grant number 2031227.

Data Availability Statement: The raw data supporting the conclusions of this article will be made available by the authors on request.

Acknowledgments: This study was based upon work supported by the National Science Foundation under Grant No. 2031227. The authors also thank Kareem Ahmad, Juanpablo Delgado, Bernhard Stiehl, Jonathan Reyes, and Steven Schroeder for discussions throughout this research.

Conflicts of Interest: The authors declare no conflict of interest.

Nomenclature

Acronyms

CFD	Computational Fluid Dynamics
WHO	World Health Organization
HVAC	Heating, Ventilation, and Air Conditioning
OPC	Optical Particle Counting
APS	Aerodynamic Particle Sizing
SMPS	Scanning Mobility Particle Sizing
URT	Upper Respiratory Tract
DES	Detached Eddy Simulation

PSD	Particle Size Distribution
LES	Large Eddy Simulation
URANS	Unsteady Reynolds-Averaged Navier–Stokes
TAB	Taylor Analogy Breakup
Variables	
ρ	density $\left(\frac{\mathrm{kg}}{\mathrm{m}^3}\right)$
∇	grad operator
t	time (s)
$\vec{u}$	velocity field $\left(\frac{\mathrm{m}}{\mathrm{s}}\right)$
p	pressure field $\left(\frac{\mathrm{N}}{\mathrm{m}^2}\right)$
P_o	reference pressure $\left(\frac{\mathrm{N}}{\mathrm{m}^2}\right)$
$\vec{g}$	gravity vector $\left(\frac{\mathrm{m}}{\mathrm{s}^2}\right)$
$\overline{\overline{\tau}}$	shear stress tensor $\left(\frac{\mathrm{N}}{\mathrm{m}^2}\right)$
c_p	specific heat capacity at constant pressure $\left(\frac{\mathrm{J}}{\mathrm{kg}\cdot\mathrm{K}}\right)$
T	temperature (K)
k	thermal conductivity $\left(\frac{\mathrm{W}}{\mathrm{m}\cdot\mathrm{K}}\right)$
$S_{e,evap}$	energy source term during the evaporation process $\left(\frac{\mathrm{J}\cdot\mathrm{kg}}{\mathrm{s}\cdot\mathrm{m}^3}\right)$
D_n	diffusion coefficient for species n in the mixture $\left(\frac{\mathrm{m}^2}{\mathrm{s}}\right)$
Y_n	local mass fraction of species
$S_{Y,n,evap}$	mass fraction source term $\left(\frac{\mathrm{kg}}{\mathrm{m}^3\cdot\mathrm{s}}\right)$
$m._{pi}$	mass fraction of each term
I	identity tensor
E	energy per unit mass $\left(\frac{\mathrm{J}}{\mathrm{kg}}\right)$
R	ideal gas constant $\left(\frac{\mathrm{J}}{\mathrm{K}\cdot\mathrm{mol}}\right)$
We	Weber number, $\frac{\rho U_{rel}^2 D}{\sigma}$
We_{crit}	critical Weber number
μ_t	turbulent viscosity (Pa·s)
Pr_t	turbulent Prandtl number, $\frac{C_p \mu_t}{k_t}$
Sc_t	turbulent Schmidt number, $\frac{\mu_t}{\rho D_t}$
D_n	diffusion coefficient $\left(\frac{\mathrm{m}^2}{\mathrm{s}}\right)$
Oh	Ohnesorge number, $\frac{\mu_d}{\sqrt{\rho_d D \sigma}}$
U_{rel}	relative velocity between droplet and flow medium $\left(\frac{\mathrm{m}}{\mathrm{s}}\right)$
D	droplet diameter (m)
σ	surface tension of droplet $\left(\frac{\mathrm{N}}{\mathrm{m}}\right)$
μ_d	droplet dynamic viscosity (Pa·s)
$m.$	rate of mass change $\left(\frac{\mathrm{kg}}{\mathrm{s}}\right)$
B	Spalding transfer number, $\frac{c_p\left(T-T_p\right)}{L}$
g^*	mass transfer conductance $\left(\frac{\mathrm{kg}}{\mathrm{m}^3}\right)$

References

1. Available online: https://www.who.int/emergencies/diseases/novel-coronavirus-2019/advice-for-public (accessed on 15 December 2021).
2. Dbouk, T.; Drikakis, D. On respiratory droplets and face masks. *Phys. Fluids* **2020**, *32*, 063303. [CrossRef] [PubMed]
3. Aliabadi, A.A.; Rogak, S.N.; Green, S.I.; Bartlett, K.H. CFD simulation of human coughs and sneezes: A study in droplet dispersion, heat, and mass transfer. *ASME Int. Mech. Eng. Congr. Expo. Proc.* **2010**, *7*, 1051–1060. [CrossRef]
4. Pilch, M.; Erdman, C.A. Use of breakup time data and velocity history data to predict the maximum size of stable fragments for acceleration-induced breakup of a liquid drop. *Int. J. Multiph. Flow* **1987**, *13*, 741–757. [CrossRef]
5. Omidvar, A. Development and assessment of an improved droplet breakup model for numerical simulation of spray in a turbulent flow field. *Appl. Therm. Eng.* **2019**, *156*, 432–443. [CrossRef]
6. Ortiz, C.; Joseph, D.D.; Beavers, G.S. Acceleration of a liquid drop suddenly exposed to a high-speed airstream. *Int. J. Multiph. Flow* **2004**, *30*, 217–224. [CrossRef]

7. Wells, W.F.; Stone, W.R. ON AIR-BORNE INFECTION: STUDY III. VIABILITY OF DROPLET NUCLEI INFECTION. *Am. J. Epidemiol.* **1934**, *20*, 619–627. [CrossRef]
8. Reyes, J.; Fontes, D.; Bazzi, A.; Otero, M.; Ahmed, K.; Kinzel, M. Effect of saliva fluid properties on pathogen transmissibility. *Sci. Rep.* **2021**, *11*, 1–14. [CrossRef] [PubMed]
9. Morawska, L.; Buonanno, G.; Mikszewski, A.; Stabile, L. The physics of respiratory particle generation, fate in the air, and inhalation. *Nat. Rev. Phys.* **2022**, *4*, 723–734. [CrossRef] [PubMed]
10. Seminara, G.; Carli, B.; Forni, G.; Fuzzi, S.; Mazzino, A.; Rinaldo, A. Biological fluid dynamics of airborne COVID-19 infection. *Rend. Lincei. Sci. Fis. e Nat.* **2020**, *31*, 8. [CrossRef]
11. Chao, C.Y.H.; Wan, M.P.; Morawska, L.; Johnson, G.R.; Ristovski, Z.D.; Hargreaves, M.; Mengersen, K.; Corbett, S.; Li, Y.; Xie, X.; et al. Characterization of expiration air jets and droplet size distributions immediately at the mouth opening. *J. Aerosol Sci.* **2009**, *40*, 122–133. [CrossRef]
12. Wang, H.; Li, Z.; Zhang, X.; Zhu, L.; Liu, Y.; Wang, S. The motion of respiratory droplets produced by coughing. *Phys. Fluids* **2020**, *32*, 125102. [CrossRef] [PubMed]
13. Mittal, R.; Meneveau, C.; Wu, W. A mathematical framework for estimating risk of airborne transmission of COVID-19 with application to face mask use and social distancing. *Phys. Fluids* **2020**, *32*, 101903. [CrossRef] [PubMed]
14. Katre, P.; Banerjee, S.; Balusamy, S.; Sahu, K.C. Fluid dynamics of respiratory droplets in the context of COVID-19: Airborne and surfaceborne transmissions. *Phys. Fluids* **2021**, *33*, 081302. [CrossRef]
15. Stiehl, B.; Shrestha, R.; Schroeder, S.; Delgado, J.; Bazzi, A.; Reyes, J.; Kinzel, M.; Ahmed, K. The effect of relative air humidity on the evaporation timescales of a human sneeze COLLECTIONS The effect of relative air humidity on the evaporation timescales of a human sneeze. *AIP Adv.* **2022**, *12*, 75210. [CrossRef] [PubMed]
16. Wang, B.; Wu, H.; Wan, X.F. Transport and fate of human expiratory droplets—A modeling approach. *Phys. Fluids* **2020**, *32*, 083307. [CrossRef] [PubMed]
17. Kumar, S. Insight on the evaporation dynamics in reducing the COVID-19 infection triggered by respiratory droplets. *Phys. Fluids* **2021**, *33*, 072004. [CrossRef]
18. Schroeder, S.; Stiehl, B.; Delgado, J.; Shrestha, R.; Kinzel, M.; Ahmed, K. Interactions of Aerosol Droplets with Ventilated Airflows in the Context of Airborne Pathogen Transmission. In Proceedings of the ASME 2022 Fluids Engineering Division Summer Meeting, Toronto, ON, Canada, 3–5 August 2022; pp. 1–8. [CrossRef]
19. Downing, G.H.; Hardalupas, Y.; Archer, J.; Symons, H.E.; Baloglu, U.B.; Schien, D.; Bzdek, B.R.; Reid, J.P. Computational and Experimental Study of Aerosol Dispersion in a Ventilated Room. *Aerosol Sci. Technol.* **2022**, *57*, 50–62. [CrossRef]
20. Craven, B.A.; Settles, G.S. A computational and experimental investigation of the human thermal plume. *J. Fluids Eng. Trans. ASME* **2006**, *128*, 1251–1258. [CrossRef]
21. Mohamadi, F.; Fazeli, A. A Review on Applications of CFD Modeling in COVID-19 Pandemic. *Arch. Comput. Methods Eng.* **2022**, *29*, 3567–3586. [CrossRef] [PubMed]
22. Liu, H.; He, S.; Shen, L.; Hong, J. Simulation-based study of COVID-19 outbreak associated with air-conditioning in a restaurant. *Phys. Fluids* **2021**, *33*, 023301. [CrossRef] [PubMed]
23. Narayanan, S.R.; Yang, S. Airborne transmission of virus-laden aerosols inside a music classroom: Effects of portable purifiers and aerosol injection rates. *Phys. Fluids* **2021**, *33*, 033307. [CrossRef] [PubMed]
24. Ramajo, D.E.; Corzo, S. Airborne Transmission Risk in Urban Buses: A Computational Fluid Dynamics Study. *Aerosol Air Qual. Res.* **2022**, *22*, 210334. [CrossRef]
25. Schreck, J.H.; Lashaki, M.J.; Hashemi, J.; Dhanak, M.; Verma, S. Aerosol generation in public restrooms. *Phys. Fluids* **2021**, *33*, 033320. [CrossRef] [PubMed]
26. Foster, A.; Kinzel, M. SARS-CoV-2 transmission in classroom settings: Effects of mitigation, age, and Delta variant. *Phys. Fluids* **2021**, *33*, 113311. [CrossRef] [PubMed]
27. Fontes, D.; Reyes, J.; Ahmed, K.; Kinzel, M. A study of fluid dynamics and human physiology factors driving droplet dispersion from a human sneeze. *Phys. Fluids* **2020**, *32*, 111904. [CrossRef] [PubMed]
28. Krishnaprasad, K.A.; Zgheib, N.; Choudhary, K.; Ha, M.Y.; Choi, C.Y.; Bang, K.S.; Jang, S.; Balachandar, S. Existence of a Nonzero Worst-Case ACH for Short-Term Exposure in Ventilated Indoor Spaces. *Indoor Air* **2024**, *2024*, 6642205. [CrossRef]
29. Sarhan, A.A.R.; Naser, P.; Naser, J. Numerical study of when and who will get infected by coronavirus in passenger car. *Environ. Sci. Pollut. Res.* **2022**, *29*, 57232–57247. [CrossRef] [PubMed]
30. Sarhan, A.A.R.; Naser, P.; Naser, J. Aerodynamic Prediction of Time Duration to Becoming Infected with Coronavirus in a Public Place. *Fluids* **2022**, *7*, 176. [CrossRef]
31. Sarhan, A.R.; Naser, P.; Naser, J. COVID-19 aerodynamic evaluation of social distancing in indoor environments, a numerical study. *J. Environ. Health Sci. Eng.* **2021**, *19*, 1969–1978. [CrossRef]
32. Hall, D. The Relationship of Fabric Properties and Bacterial Filtration Efficiency for Selected Surgical Face Masks. No. January 2003. 2014. Available online: https://www.researchgate.net/publication/242297437_The_Relationship_of_Fabric_Properties_and_Bacterial_Filtration_Efficiency_for_Selected_Surgical_Face_Masks (accessed on 21 September 2024).
33. Drewnick, F.; Pikmann, J.; Fachinger, F.; Moormann, L.; Sprang, F.; Borrmann, S. Aerosol filtration efficiency of household materials for homemade face masks: Influence of material properties, particle size, particle electrical charge, face velocity, and leaks. *Aerosol Sci. Technol.* **2021**, *55*, 63–79. [CrossRef]

34. Siemens Digital Industries Software. Simcenter STAR-CCM+, Siemens. 2021. Available online: https://www.plm.automation.siemens.com/global/en/%0Aproducts/simcenter/STAR-CCM.html (accessed on 21 September 2024).
35. Han, Z.Y.; Weng, W.G.; Huang, Q.Y.; Han, Z.Y.; Huang, Q.Y. Characterizations of particle size distribution of the droplets exhaled by sneeze. *J. R. Soc. Interface* **2013**, 10. [CrossRef]
36. Li, H.; Liu, S.M.; Yu, X.H.; Tang, S.L.; Tang, C.K. Coronavirus disease 2019 (COVID-19): Current status and future perspectives. *Int. J. Antimicrob. Agents* **2020**, *55*, 105951. [CrossRef] [PubMed]
37. Spalart, P.R. Comments on the Feasibility of LES for Wings, and on a Hybrid RANS/LES Approach. January 1997, Conference: Advances in DNS/LES. Available online: https://www.researchgate.net/publication/236888805_Comments_on_the_Feasibility_of_LES_for_Wings_and_on_a_Hybrid_RANSLES_Approach (accessed on 21 September 2024).
38. Continescu, G.; Pacheco, R.; Squires, K. Detached-eddy simulation of flow over a sphere. In Proceedings of the 40th AIAA Aerospace Sciences Meeting & Exhibit, Reno, NV, USA, 14–17 January 2002; p. 425.
39. Spalart, P.; Allmaras, S. A one-equation turbulence model for aerodynamic flows. In Proceedings of the 30th Aerospace Sciences Meeting and Exhibit, Reno, NV, USA, 6–9 January 1992.
40. Schiller, L. Über die grundlegenden Berechnungen bei der Schwerkraftaufbereitung. *Z. Vereines Dtsch. Inge.* **1933**, *77*, 318–321.
41. Ranz, W.E. Evaporation from drops, Parts I & II. *Chem. Eng. Process.* **1952**, 141–146. Available online: https://www.semanticscholar.org/paper/Evaporation-from-drops-Ranz/e3fa177e8eb44fb0cc81e57895d93b19e605be5d (accessed on 21 September 2024).
42. Scharfman, B.E.; Techet, A.H.; Bush, J.W.M.; Bourouiba, L. Visualization of sneeze ejecta: Steps of fluid fragmentation leading to respiratory droplets. *Exp. Fluids* **2016**, *57*, 24. [CrossRef] [PubMed]
43. Guildenbecher, D.R.; López-Rivera, C.; Sojka, P.E. Secondary atomization. *Exp. Fluids* **2009**, *46*, 371–402. [CrossRef]
44. O'Rourke, P.; Amsden, A. The TAB Method for Numerical Calculation of Spray Droplet Breakup. In Proceedings of the SAE International Fall Fuels and Lubricants Meeting and Exposition, Toronto, ON, Canada, 2–5 November 1987; Available online: https://digital.library.unt.edu/ark:/67531/metadc1106123/m1/1/ (accessed on 21 September 2024).
45. Gidreta, B.T.; Kim, H. Effects of physical property changes of expelled respiratory liquid on atomization morphology. *J. Fluid Mech.* **2023**, *960*, 1–12. [CrossRef]

Disclaimer/Publisher's Note: The statements, opinions and data contained in all publications are solely those of the individual author(s) and contributor(s) and not of MDPI and/or the editor(s). MDPI and/or the editor(s) disclaim responsibility for any injury to people or property resulting from any ideas, methods, instructions or products referred to in the content.